

1 **Do surface lateral flows matter for data assimilation of soil moisture observations**
2 **into hyperresolution land models?**

3 **Running title: HYPERRESOLUTION LAND DATA ASSIMILATION**

4 Yohei Sawada¹,

5 ¹ Meteorological Research Institute, Japan Meteorological Agency, Tsukuba, Japan

6
7 Corresponding author: Y. Sawada, Meteorological Research Institute, Japan
8 Meteorological Agency, 1-1, Nagamine, Tsukuba, Japan, ysawada@mri-jma.go.jp

9
10 **Key Points:**

- 11 1. Surface lateral flows matter when soil moisture observations are assimilated into
12 high-resolution integrated surface-groundwater land models.
13 2. The efficiency of an ensemble Kalman filter to assimilate soil moisture observations
14 depends on soil characteristics.

15
16 **Keywords:** data assimilation, hyperresolution land model, soil moisture

17
18 **Abstract**

19 Hyperresolution land modeling is expected to innovate the simulation of terrestrial water,
20 energy, and carbon cycles. One of the major advantages of existing hyperresolution land
21 models against conventional 1-dimensional land surface models is that surface and
22 subsurface lateral water flows can be explicitly simulated. Despite a lot of efforts on
23 assimilating hydrological observations into the hyperresolution integrated surface-
24 groundwater land models, how and in what case topography-driven surface water flows
25 matter for data assimilation of soil moisture observations has yet to be clarified. In this
26 study, I perform a minimalist synthetic numerical experiment, in which shallow soil
27 moisture observations are assimilated into an integrated surface-groundwater land model
28 by the ensemble Kalman filter. Propagation of a model error due to surface lateral water
29 flows is crucially important to adjust the unobserved model state and parameter variables
30 by horizontally propagating the information of soil moisture observations. However, the
31 non-Gaussianity of the model error induced by the nonlinear dynamics of topography-
32 driven surface flows harms the performance of an ensemble Kalman filter and the
33 efficiency of data assimilation strongly depends on soil characteristics. The new
34 capability of data assimilation with the hyperresolution land models found in this study
35 may improve the monitoring and prediction of flash floods caused by local severe rainfalls.

36

37

38 **1. Introduction**

39 Hyperresolution land modeling is expected to innovate the simulation of terrestrial water,
40 energy, and carbon cycles, which is crucially important for meteorological, hydrological
41 and ecological applications. While conventional land surface models (LSMs) assume that
42 lateral water flows are negligible at a coarse resolution and solve vertical 1-dimensional
43 Richards equation for the soil moisture simulation (e.g., Sellers et al. 1996; Lawrence et
44 al. 2011), currently proposed hyperresolution land models, which can be applied at a finer
45 resolution (<1km), explicitly consider surface and subsurface lateral water flows (e.g.,
46 Maxwell and Miller 2005; Tian et al. 2012; Shrestha et al. 2014; Niu et al. 2014). Previous
47 works indicated that a lateral transport of water plays important roles in terrestrial water
48 and energy cycles (e.g., Maxwell and Condon 2016; Ji et al. 2017; Fang et al. 2017) and
49 land-atmosphere interactions (e.g., Williams and Maxwell 2011; Keune et al. 2016).

50

51 Data assimilation has contributed to improving the performance of LSMs by fusing
52 simulation and observation. The grand challenge of land data assimilation is to estimate
53 unobservable variables from observations by propagating observations' information into
54 model's high dimensional state and parameter space. In previous works on the
55 conventional 1-D LSMs, many land data assimilation systems (LDASs) have been
56 proposed to accurately estimate model's state and parameter variables, which cannot be
57 directly observed, by assimilating satellite and in-situ observations. For example, the
58 optimization of LSM's unknown parameters (e.g., hydraulic conductivity) has been
59 implemented by assimilating remotely sensed microwave observations (e.g., Yang et al.
60 2007; Yang et al. 2009; Bandara et al. 2014; Bandara et al. 2015; Sawada and Koike 2014;
61 Han et al. 2014). Kumar et al. (2009) analyzed the simulated correlation between surface
62 soil moisture and root-zone soil moisture to improve the simulation of root-zone soil
63 moisture by assimilating remotely sensed surface soil moisture observations. Sawada et
64 al. (2015) successfully improved the simulation of root-zone soil moisture by assimilating
65 microwave brightness temperature observations which include the information of
66 vegetation water content. Gravity Recovery and Climate Experiment total water storage
67 observation has been intensively used to improve the simulation of groundwater and soil
68 moisture (e.g., Li et al. 2012; Houborg et al. 2012). Improving the simulation of state
69 variables such as soil moisture and biomass by LDASs has contributed to accurately
70 estimating fluxes such as evapotranspiration (e.g. Martens et al. 2017) and CO2 flux (e.g.,
71 Verbeeck et al. 2011). However, in most of the studies on the conventional 1-D LDASs,
72 observations impacted state and parameter variables only in a single model's horizontal

73 grid which is identical to the location of the observation. The assumption that the surface
74 and subsurface water flows are restricted to vertical direction in LSMs makes it difficult
75 to propagate observation's information horizontally, which limits the potential of land
76 data assimilation to fully use land hydrological observations.

77

78 The hyperresolution land models, which explicitly solve surface and subsurface lateral
79 flows, provide a unique opportunity to examine the potential of land data assimilation to
80 propagate observation's information horizontally in a model space and efficiently use
81 land hydrological observations. Previous works successfully applied Ensemble Kalman
82 Filters (EnKF) to 3-D Richards' equation-based integrated surface-groundwater models.
83 For example, Camporese et al. (2009) and Camporese et al. (2010) successfully
84 assimilated the synthetic observations of surface pressure head and streamflow into the
85 Catchment Hydrology (CATHY). Kurtz et al. (2016) coupled the Parallel Data
86 Assimilation Framework (PDAF) (Nerger and Hiller 2013) with the Terrestrial System
87 Modelling Framework (TerrSysMP) (Shrestha et al. 2014). The performance of
88 TerrSysMP-PDAF to assimilate soil moisture observations was evaluated by a simple
89 synthetic experiment (see also Zhang et al. (2018)).

90

91 Although the data assimilation of hydrological observations into the hyperresolution land
92 models has been successfully implemented in the synthetic experiments, it is unclear how
93 and in what case topography-driven surface lateral water flows matter for data
94 assimilation of soil moisture observations. Previous studies on data assimilation with high
95 resolution models mainly focused on assimilating groundwater observations (e.g., Ait-El-
96 Fquih et al. 2016; Rasmussen et al. 2015; Hendricks-Franssen et al. 2008). There are some
97 applications which focused on the observation of soil moisture and pressure head in
98 shallow unsaturated soil layers. However, in those literatures, topography-driven surface
99 flows have not been considered in the experiment (Kurtz et al. 2016) or the role of them
100 in assimilating observations into the hyperresolution land models has not been
101 quantitatively discussed (Camporese et al. 2010; Camporese et al. 2009). This study aims
102 at clarifying if surface lateral flows matter for data assimilation of soil moisture
103 observations into hyperresolution land models by a minimalist numerical experiment.

104

105

106

107

108

109 2. Methods

110 2.1. Model

111 ParFlow is an open source platform which realizes fully integrated surface-groundwater
112 flow modeling (Kollet and Maxwell 2006; Maxwell et al. 2015). This parallel simulation
113 platform has been widely used as a core hydrological module in hyperresolution land
114 models (e.g., Maxwell and Kollet 2008; Maxwell and Condon 2016; Fang et al. 2017;
115 Kurtz et al. 2016; Maxwell et al. 2011; Williams and Maxwell 2011; Shrestha et al. 2014).
116 The brief description on the method of ParFlow to simulate integrated surface-subsurface
117 water flows can be found below and the complete description of ParFlow can be found in
118 Kollet and Maxwell (2006), Maxwell et al. (2015) and references therein.

119

120 In the subsurface, ParFlow solves the variably saturated Richards equation in three
121 dimensions.

$$122 S_S S_W(h) \frac{\partial h}{\partial t} + \phi S_W(h) \frac{\partial S_W(h)}{\partial t} = \nabla \cdot \mathbf{q} + q_r \quad (1)$$

$$123 \mathbf{q} = -\mathbf{K}_s(\mathbf{x}) k_r(h) [\nabla(h+z) \cos\theta_x + \sin\theta_x] \quad (2)$$

124 In equation (1), h is the pressure head [L]; z is the elevation with the z axis specified as
125 upward [L]; S_S is the specific storage [L^{-1}]; S_W is the relative saturation; ϕ is the
126 porosity [-]; q_r is a general source/sink term. Equation (2) describes the flux term \mathbf{q}
127 [LT^{-1}] based on Darcy's law, and \mathbf{K}_s is the saturated hydraulic conductivity tensor [LT^{-1}];
128 k_r is the relative permeability [-]; θ is the local angle of topographic slope (see
129 Maxwell et al. 2015). In this paper, the saturated hydraulic conductivity is assumed to be
130 isotropic and the function of z :

$$131 \mathbf{K}_s = K_s(z) = K_{s,surface} \exp(-f(z_{surface} - z)) \quad (3)$$

132 where $K_{s,surface}$ is the saturated hydraulic conductivity at the soil surface, and $z_{surface}$
133 is the elevation of the soil surface. The saturated hydraulic conductivity decreases
134 exponentially as the soil depth increases (Beven 1982). The van Genuchten relationship
135 (van Genuchten 1980) is used to describe the relative saturation and permeability
136 functions.

137

138 Overland flow is solved by the two-dimensional kinematic wave equation. The dynamics
139 of the surface ponding depth, h [L], can be described by:

$$140 \mathbf{k} \cdot [-K_s(z) k_r(h) \cdot \nabla(h+z)] = \frac{\partial \|h, 0\|}{\partial t} - \nabla \cdot \|h, 0\| \mathbf{v}_{sw} + q_r \quad (4)$$

141 In equation (4), \mathbf{k} is the unit vector in the vertical and $\|a, b\|$ indicates the greater value
142 of the two quantities following the notation of Maxwell et al. (2015). If $h < 0$, equation

143 (4) describes that vertical fluxes across the land surface boundary is equal to a general
 144 source/sink term q_r (i.e., rainfall and evapotranspiration). If $h > 0$, the terms on the right-
 145 hand side of equation (4), which indicates water fluxes routed according to surface
 146 topography, are active. \mathbf{v}_{sw} is the two-dimensional depth-averaged overland flow
 147 velocity [LT^{-1}] and estimated by the Manning's law:

$$148 \quad \mathbf{v}_{sw} = \left(\begin{array}{c} \frac{\sqrt{S_{f,x}}}{n} h^{\frac{2}{3}} \\ \frac{\sqrt{S_{f,y}}}{n} h^{\frac{2}{3}} \end{array} \right) \quad (5)$$

149 where $S_{f,x}$ and $S_{f,y}$ are the friction slopes [-] for the x- and y-direction, respectively; n
 150 is the Manning's coefficient [$TL^{-1/3}$]. In the kinematic wave approximation, the friction
 151 slopes are set to the bed slopes. The methodology of discretization and numerical
 152 implementation to solve equations (1-5) can be found in Kollet and Maxwell (2006).

153
 154

155 2.2. Data Assimilation

156 In this paper, the ensemble Kalman filter (EnKF) was applied to assimilate soil moisture
 157 observations into ParFlow. The general description of the Kalman filter is the following:

$$158 \quad \mathbf{x}^f(t) = \mathcal{M}[\mathbf{x}^a(t-1)] \quad (6)$$

$$159 \quad \mathbf{x}^a(t) = \mathbf{x}^f(t) + \mathbf{K}[y^o - \mathcal{H}\mathbf{x}^f(t)] \quad (7)$$

$$160 \quad \mathbf{K} = \mathbf{P}^f \mathcal{H}^T (\mathcal{H} \mathbf{P}^f \mathcal{H}^T + \mathbf{R})^{-1} \quad (8)$$

$$161 \quad \mathbf{P}^a = (\mathbf{I} - \mathbf{K} \mathcal{H}) \mathbf{P}^f \quad (9)$$

162 I follow the notation of Houtekamer and Zhang (2016). In equation (6), a forecast model
 163 \mathcal{M} (ParFlow in this study) is used to obtain a prior estimate at time t , $\mathbf{x}^f(t)$, from the
 164 estimation at the previous time $\mathbf{x}^a(t-1)$. In equation (7), a prior estimate $\mathbf{x}^f(t)$ is
 165 updated to the analysis state, $\mathbf{x}^a(t)$, using new observations y^o . The Kalman gain matrix
 166 \mathbf{K} calculated by equation (8) is used to give an appropriate weight between the
 167 observations with an error covariance matrix \mathbf{R} , and the prior with an error covariance
 168 matrix \mathbf{P}^f . To calculate \mathbf{K} , the observation operator \mathcal{H} is needed to map from model
 169 space to observation space. It should be noted that the equations (6-9) give an optimal
 170 estimation only when the error in model and observation follows the Gaussian distribution.
 171 When the probabilistic distribution of the error in either model or observation has non-
 172 Gaussian structure, results of the Kalman filter are suboptimal. This point is important to
 173 interpret the results of this study.

174

175 EnKF is the Monte Carlo implementation of equations (6-9). To compute the Kalman gain
 176 matrix, \mathbf{K} , ensemble approximations of $\mathbf{P}^f \mathcal{H}^T$ and $\mathcal{H} \mathbf{P}^f \mathcal{H}^T$ can be given by:

177 $\mathbf{P}^f \mathcal{H}^T \equiv \frac{1}{k-1} \sum_{i=1}^k (x_i^f - \overline{x^f}) (\mathcal{H} x_i^f - \overline{\mathcal{H} x^f})^T$ (10)

178 $\mathcal{H} \mathbf{P}^f \mathcal{H}^T \equiv \frac{1}{k-1} \sum_{i=1}^k (\mathcal{H} x_i^f - \overline{\mathcal{H} x^f}) (\mathcal{H} x_i^f - \overline{\mathcal{H} x^f})^T$ (11)

179 where x_i^f is the i th member of a k -member ensemble prior and $\overline{x^f} = \frac{1}{k} \sum_{i=1}^k x_i^f$ and

180 $\overline{\mathcal{H} x^f} = \frac{1}{k} \sum_{i=1}^k \mathcal{H} x_i^f$.

181

182 Once $\overline{x^a} = \sum_{i=1}^k x_i^a$ (x_i^a is the i th member of a k -member ensemble analysis) and $\mathbf{P}^a =$

183 $\frac{1}{k-1} \sum_{i=1}^k (x_i^a - \overline{x^a}) (x_i^a - \overline{x^a})^T$ are computed by equations (6-11), there are still many

184 possible choices of an analysis ensemble. There are many proposed flavors of EnKF and

185 one of the main differences among them is how to choose the analysis ensemble x_i^a . In

186 this paper, the Ensemble Transform Kalman Filter (ETKF; Bishop et al. 2001; Hunt et al.

187 2007) was used to transport forecast ensembles to analysis ensembles.

188

189 In the ETKF, the analysis update for an ensemble mean is done by the following
190 equations:

191 $\tilde{\mathbf{P}}^a = [(k-1)I + (Y^f)^T R^{-1} Y^f]^{-1}$ (12)

192 $\overline{w}^a = \tilde{\mathbf{P}}^a (Y^f)^T R^{-1} (y^o - \overline{y^f})$ (13)

193 $\overline{x^a} = \overline{x^f} + X^f \overline{w}^a$ (14)

194 where the i th columns of Y^f and X^f are $y_i^f - \overline{y^f}$ and $x_i^f - \overline{x^f}$, respectively. y_i^f is
195 defined by $y_i^f = \mathcal{H} x_i^f$ and $\overline{y^f}$ is the ensemble mean of y_i^f . I is the identity matrix.

196

197 The analysis covariance \mathbf{P}^a is given by:

198 $\mathbf{P}^a = \frac{1}{k-1} X^a (X^a)^T = X^f \tilde{\mathbf{P}}^a (X^f)^T$ (15)

199 where the i th column of X^a is $x_i^a - \overline{x^a}$. The perturbations of the analysis ensemble
200 members can be generated by the square root of $\tilde{\mathbf{P}}^a$:

201 $W^a = [(k-1)\tilde{\mathbf{P}}^a]^{1/2}$ (16)

202 $X^a = X^f W^a$ (17)

203 Please refer to Hunt et al. (2007) for the complete description of the ETKF and its
204 localized version, the Local Ensemble Transform Kalman Filter (LETKF).

205

206 In many ensemble Kalman filter systems, the ensemble spread tends to become
207 underdispersive without any ensemble inflation methods (Houtekamer and Zhang, 2016).
208 In this paper, the relaxation to prior perturbation method (RTPP) of Zhang et al. (2004)
209 was used to maintain an appropriate ensemble spread. In the RTPP, the computed analysis
210 perturbations are relaxed back to the forecast perturbations:

$$211 x_{i,new}^a = (1 - \alpha)(x_i^a - \bar{x}^a) + \alpha(x_i^f - \bar{x}^f), \quad 0 \leq \alpha \leq 1 \quad (18)$$

212 where α was set to 0.975 in this study.

213

214

215 **3. Experiment Design**

216 The synthetic experiment was implemented to examine how topography-driven surface
217 lateral flows contribute to efficiently propagating observation's information horizontally
218 in the data assimilation of soil moisture observation. Two synthetic reference runs were
219 created by Parflow. The 2-D domain has a horizontal extension of 4000m and a vertical
220 extension of 5m. The domain of the virtual slope was horizontally discretized into 40 grid
221 cells with a grid cell size of 100m and vertically discretized into 50 grid cells with a grid
222 cell size of 0.10m. The domain has a 25% slope. In two synthetic reference runs, it heavily
223 rains only in the upper half of the slope ($2000\text{m} < x < 4000\text{m}$). A constant rainfall rate of
224 50mm/h was applied for 3 hours and then the period with no rainfall and evaporation of
225 0.075mm/h lasted for 117 hours. This 120-hour rain/no rain cycle was repeatedly applied
226 to the domain. The configurations described above were schematically shown in Figure
227 1a. The parameters of the van Genuchten relationship, alpha and n, were set to 1.5 and
228 1.75, respectively. The porosity, ϕ in equation (1), was set to 0.40. The Manning's
229 coefficient, n in equation (5), was set to 5.52×10^{-6} [$\text{m}^{-1/3}\text{h}$]. The initial groundwater
230 table was located in $z=3\text{m}$ and the hydrostatic pressure gradient was assumed for the
231 initial pressure heads in the unsaturated soil layers.

232

233 The difference between two synthetic reference runs is the value of saturated hydraulic
234 conductivity. The surface saturated hydraulic conductivity, $K_{s,surface}$ in equation (3),
235 was set to 0.005 [m/h] in one reference, and 0.02 [m/h] in the other. Figure 1 shows the
236 difference of the response to heavy rainfall between the two synthetic reference runs. In
237 the case of the low saturated hydraulic conductivity (hereafter called the LOW_K
238 reference), larger surface lateral flows are generated than the case of the high saturated
239 hydraulic conductivity (hereafter called the HIGH_K reference). In the LOW_K
240 reference, the topography-driven surface lateral flows reach the left edge of the domain
241 (Figure 1b). In the HIGH_K reference, supplied water moves vertically rather than

242 horizontally and the topography-driven surface flows reach around $x = 1000\sim 1500\text{m}$
243 (Figure 1d).

244

245 For the data assimilation experiment, an ensemble of 50 realizations were generated. Each
246 ensemble member has different saturated hydraulic conductivity and rainfall rate.
247 Lognormal multiplicative noise was added to surface saturated hydraulic conductivity
248 and rainfall rate of the synthetic reference runs. The two parameters of the lognormal
249 distribution, commonly called μ and σ , were set to 0 and 0.15, respectively. The initial
250 groundwater depth of each ensemble member was drawn from the uniform distribution
251 from 2.0m to 3.5m and the hydrostatic pressure gradient was assumed for the initial
252 pressure heads in the unsaturated soil layers.

253

254 The virtual hourly observations were generated by adding the Gaussian white noise whose
255 mean is zero to the volumetric soil moisture simulated by the synthetic reference runs.
256 The observation error (the standard deviation of the added Gaussian white noise) was set
257 to $0.05 \text{ m}^3/\text{m}^3$. It was assumed that the volumetric soil moistures can be observed in every
258 soil layer from surface to the depth of 1m at the specific location. The two scenarios of
259 the observation's location are provided. In the first scenario (hereafter called the UP_O
260 scenario), the volumetric soil moisture at the upper part of the slope ($x = 2500\text{m}$) was
261 observed. In the UP_O scenario, I could observe the volumetric soil moisture in the upper
262 part of the slope where it heavily rains and tried to infer the soil moisture in the lower part
263 of the slope where it does not rain by propagating the observation's information downhill.
264 In the second scenario (hereafter called the DOWN_O scenario), the volumetric soil
265 moisture at the lower part of the slope ($x = 1500\text{m}$) was observed. In the DOWN_O
266 scenario, I could observe the volumetric soil moisture in the lower part of the slope where
267 it does not rain and tried to infer the soil moisture in the upper part of the slope where it
268 heavily rains by propagating the observation's information uphill.

269

270 Since I had the two synthetic reference runs (the HIGH_K and LOW_K references) and
271 the two observation scenarios (the UP_O and DOWN_O scenarios), I implemented totally
272 four data assimilation experiments. Table 1 summarizes the data assimilation experiments
273 implemented in this study. For instance, in the HIGH_K-UP_O experiment, I chose the
274 HIGH_K reference and generated an ensemble of 50 realizations from the HIGH_K
275 reference. The soil moisture observations were generated from the HIGH_K reference at
276 the location of $x = 2500\text{m}$ and assimilated into the model every hour. The simulated

277 volumetric soil moisture of the data assimilation experiment was compared with that of
278 the HIGH_K reference.

279

280 In the data assimilation experiments, I adjusted pressure head by data assimilation so that
281 x^f in section 2.2 is pressure head. Since the surface saturated hydraulic conductivity was
282 also adjusted, x^f in section 2.2 includes $K_{s,surface}$. It should be noted that I adjusted a
283 single surface saturated hydraulic conductivity which is applied to the whole domain so
284 that the estimated parameter was not spatially distributed. Spatial regularization has been
285 applied to calibrate spatially distributed parameters by adjusting a single parameter
286 (Pokhrel and Gupta 2010). I suppose to apply the spatial regularization in the real-world
287 application of the hyperresolution land data assimilation. Since I assimilated volumetric
288 soil moisture observations (y^f and y^o in section 2.2 are simulated and observed
289 volumetric soil moisture, respectively), the van Genuchten relationship works as an
290 observation operator \mathcal{H} in this study.

291

292 In addition to the data assimilation (DA) experiments, I implemented the NoDA
293 experiment (also called the open-loop experiment in the literatures of the LDAS study)
294 in which the ensemble was used but no observation data were assimilated. As evaluation
295 metrics, root-mean-square-error (RMSE) was used:

296
$$RMSE = \sqrt{\frac{1}{k} \sum_{i=1}^k (F_i - T)^2} \quad (19)$$

297 where k is the ensemble number, F_i is the volumetric soil moisture simulated by the i -th
298 member in the DA or NoDA experiment, T is the volumetric soil moisture simulated by
299 the synthetic reference run.

300

301 To evaluate the impact of data assimilation, the improvement rate (IR) was defined and
302 calculated by the following equation:

303
$$IR = \frac{\overline{RMSE_{DA}} - \overline{RMSE_{NoDA}}}{\overline{RMSE_{NoDA}}} \quad (20)$$

304 where $\overline{RMSE_{DA}}$ and $\overline{RMSE_{NoDA}}$ are time-mean RMSE of the DA and NoDA
305 experiments, respectively. The negative IR indicates that data assimilation positively
306 impacts the simulation of soil moisture.

307

308 Four of 120-hour rain/no rain cycles were applied so that the computation period was 480
309 hours. The spin-up results in the first 120 hours were not used to calculate the evaluation
310 metrics.

311 **4. Results**

312 Figure 2a shows the IR of the LOW_K-UP_O experiment. The time series of the DA and
313 NoDA experiment and the synthetic reference run in the LOW_K-UP_O experiment can
314 be found in Figure S1. The data assimilation efficiently propagates the information of the
315 observations located in the upper part of the slope (see the black arrow in Figure 2a) both
316 horizontally and vertically. RMSE is reduced by data assimilation not only directly under
317 the observation but also the lower part of the slope where it does not rain. However, the
318 increase of RMSE by data assimilation can be found at the left edge of the domain, which
319 is far from the location of the observation. Please note that the impact of data assimilation
320 on the surface soil moisture simulation is small because the RMSE of the NoDA
321 experiment is already small ($\leq 0.01\text{m}^3/\text{m}^3$) there in the case of the LOW_K reference.

322

323 Figure 2b shows the IR of the LOW_K-DOWN_O experiment (see also Figure S2 for
324 time series). The IR's spatial pattern of the LOW_K-DOWN_O experiment is similar to
325 that of the LOW_K-UP_O experiment. It is promising that I can accurately infer soil
326 moisture in the region where it heavily rains from the shallow soil moisture observations
327 in the region where it does not rain.

328

329 Figure 3a shows the difference of time-mean RMSEs ($\overline{RMSE_{DA}}$ in equation (20))
330 between the LOW_K-UP_O and LOW_K-DOWN_O experiments. Although observing
331 the lower part of the slope slightly improves the soil moisture simulation at the left edge
332 of the domain compared with observing the upper part of the slope, there are few
333 differences between the UP_O and DOWN_O scenarios in the case of the LOW_K
334 reference. In the data assimilation system of this study, the soil moisture observations
335 have large representativeness and I can efficiently infer soil moisture in the soil columns
336 which are horizontally and vertically far from the observations.

337

338 Figure 2c shows the IR of the HIGH_K-UP_O experiment (see also Figure S3 for time
339 series). The data assimilation significantly reduces RMSE of the soil moisture simulation
340 directly under the observations (see the black arrow in Figure 2c), which indicates that
341 the data assimilation efficiently propagates the information of the observations vertically.
342 However, the impact of the data assimilation on the soil moisture simulation in the lower
343 part of the slope around $x=1500\text{m}$ is marginal although there are large RMSE in the NoDA
344 experiment ($>0.05\text{m}^3/\text{m}^3$) at the edge of the area where topography-driven surface flows
345 reach in the HIGH_K reference (see Figure 1d).

346

347 Figure 2d shows the IR of the HIGH_K-DOWN_O experiment (see also Figure S4 for
348 time series). Although the observations in the lower part of the slope (see the black arrow
349 in Figure 2d) significantly improve the soil moisture simulation in the downstream area
350 of the observation, the impact of the data assimilation on the shallow soil moisture
351 simulation around $x=500\sim 1000\text{m}$ is marginal. As I found in the LOW_K-DOWN_O
352 experiment, the shallow soil moisture observations in the region where it does not rain
353 can improve the soil moisture simulation in the region where it heavily rains. However,
354 the IR of the HIGH_K-DOWN_O experiment in the upper part of the slope is smaller
355 than that of the LOW_K-DOWN_O experiment (see Figure 2b and 2d).

356

357 The high representativeness of the observations which I found in the case of the LOW_K
358 reference cannot be found in the case of the HIGH_K reference. Figure 3b shows the
359 difference of time-mean RMSEs (\overline{RMSE}_{DA} in equation (20)) between the HIGH_K-
360 UP_O and HIGH_K-DOWN_O experiments. Compared with the LOW_K reference case
361 (Figure 3a), there are significant differences between the UP_O and DOWN_O scenarios
362 in the case of higher saturated hydraulic conductivity. In this case, the vertical propagation
363 of the observations' information is more efficient than the horizontal propagation.

364

365 The relatively low efficiency of the data assimilation and the low representativeness of
366 the soil moisture observations in the case of the HIGH_K reference are caused by the
367 non-Gaussian model error distribution. To evaluate the non-Gaussianity of the model
368 error sampled by an ensemble, I used the Kullback-Leibler divergence (KLD) (Kullback
369 and Leibler 1951):

$$370 \quad D_{KL}(p, q) = \sum_i p(i) \log \frac{p(i)}{q(i)} \quad (21)$$

371 where $D_{KL}(p, q)$ is the KLD between two probabilistic distribution functions (PDFs), p
372 and q . If two PDFs are equal for all i , $D_{KL}(p, q) = 0$. A large value for $D_{KL}(p, q)$
373 indicates that p and q are not close to each other. Therefore, the KLD is appropriate as
374 a benchmark to evaluate the closeness of two PDFs. It should be noted that the KLD is
375 not symmetric ($D_{KL}(p, q) \neq D_{KL}(q, p)$). In this study, I compared the PDF of the NoDA
376 ensemble (p in equation (21)) with the Gaussian PDF which has the mean and variance
377 of the NoDA ensemble (q in equation (21)).

378

379 Figure 4 shows that the NoDA ensemble in the case of the HIGH_K reference has stronger
380 non-Gaussianity than the case of the LOW_K reference especially in the shallow soil
381 layers. The strong non-Gaussianity of the NoDA ensemble generated from the HIGH_K

382 reference can be found at the edge of the area where topography-driven surface flows
383 reach (Figure 1d). Figure 5 shows that there is the bifurcation of the ensemble in this
384 region when the ensemble is generated from the HIGH_K reference. The process of
385 topography-driven surface flows is switched on if and only if the surface soil is saturated
386 (see equation (4)) so that the ensemble tends to be bifurcated into the members with
387 surface flows and without surface flows. As I mentioned in section 2.2, in the ETKF, the
388 state and parameter variables are adjusted assuming the Gaussian PDF of the model's
389 error and the linear relationship between observed variables and unobserved variables.
390 Therefore, the non-Gaussianity of the prior ensemble induced by the strong non-linear
391 dynamics of surface lateral flows makes the ETKF inefficient. It should be noted that the
392 non-Gaussianity can also be found in the LOW_K reference at the edge of the domain
393 ($x=500\text{m}$) due to the non-linear dynamics, which causes the degradation of the soil
394 moisture simulation in the LOW_K-UP_O experiment (see Figure 2a).

395

396

397 **5. Discussion**

398 In this study, I revealed that the hyperresolution integrated surface-subsurface
399 hydrological model gives the unique opportunity to effectively use soil moisture
400 observations to improve the soil moisture simulation. I found that the explicit calculation
401 of topography-driven surface flows has an important role in propagating the information
402 of soil moisture observation horizontally by data assimilation even if there is considerable
403 heterogeneity of meteorological forcing. It is possible that the soil moisture observations
404 in the area where it does not heavily rain can improve the soil moisture simulation in the
405 severe rainfall area. This potential cannot be brought out in the conventional 1-D LSM
406 where sub-grid scale surface runoff is parameterized and the surface flows in one grid do
407 not move to the adjacent grids. This new potential of hyperresolution land data
408 assimilation is expected to be useful to monitor and predict flash floods induced by local
409 severe rainfall on complex terrain.

410

411 However, I also found that the conventional ensemble data assimilation (i.e. ETKF)
412 severely suffers from the non-Gaussian model error PDFs caused by the strongly
413 nonlinear dynamics of topography-driven surface flows. The efficiency of ETKF to
414 propagate the information of observations horizontally in the model space is limited when
415 capacity of soil to hold water is high (i.e. high saturated hydraulic conductivity). It should
416 be noted that the low representativeness of the soil moisture observations in the case of
417 the HIGH_K reference is due to the core assumption of the Kalman filter that the error

418 PDFs follow the Gaussian distribution so that the increase of the ensemble size cannot
419 solve this issue. I implemented the data assimilation experiment in the case of the
420 HIGH_K reference with the 500 ensemble size, which is 10 times larger than the
421 experiments shown in section 4, and found no significant improvement of the soil
422 moisture simulation (not shown).

423

424 The results of the HIGH_K-UP_O and the HIGH_K-DOWN_O imply that the spatially
425 dense soil moisture observations are needed to efficiently constrain state variables at the
426 edge of surface flows. High resolution soil moisture remote sensing based on satellite
427 active and passive combined microwave observations (e.g., He et al. 2018) and the
428 assimilation of those data (Lievens et al. 2017) may be the important technologies in the
429 era of the hyperresolution land modeling. The high resolution observations of surface
430 inundated water from satellite imagery (e.g., Sakamoto et al. 2007 RSE; Arnesen et al.
431 2013 RSE) may also be useful.

432

433 Since there is the nonlinear relationship between observed and unobserved variables
434 sampled by an ensemble, a localization method, which spatially restricts the impact of
435 assimilating observation, is crucially needed for the real-world application. The results of
436 this study imply that the optimal localization radius strongly depends on the model
437 parameter (i.e. saturated hydraulic conductivity). Rasmussen et al. (2015) successfully
438 applied the adaptive localization method (Anderson 2007; Bishop and Hodyss 2009) to
439 the data assimilation of groundwater observations into a hydrological model. It is
440 appropriate to adaptively determine the localization radius considering the lack of prior
441 knowledge of how soil moistures simulated by an ensemble are horizontally correlated.

442

443 Reducing the uncertainty in rainfall positively impacts the efficiency of data assimilation
444 since the bifurcation of simulated soil moisture found in Figure 5c is originally induced
445 by the uncertainty in rainfall. Although assimilating land hydrological observations to
446 improve the rainfall input has been intensively investigated (e.g., Sawada et al. 2018;
447 Herrnegger et al. 2015; Crow et al. 2011; Vrugt et al. 2008), it has yet to be applied to the
448 hyperresolution land models. It should be noted that the parameters of the lognormal
449 distribution to model the uncertainty in rainfall were specified to make the rainfall PDF
450 similar to the Gaussian distribution. I chose the lognormal distribution in order not to
451 generate the negative value of rainfall and I did not intend to introduce non-Gaussianity
452 into the external forcing. The rainfall input which follows the Gaussian PDF was

453 transformed into the non-Gaussian PDF of the model error by the strongly nonlinear
454 dynamics of topography-driven surface flows.

455

456 To explicitly consider the non-Gaussianity and non-linear relationship between observed
457 and unobserved variables induced by topography-driven surface flows, the particle filters
458 may be useful. The particle filtering can represent a probability distribution (including
459 non-Gaussian distributions) directly by an ensemble. The particle filters have been
460 intensively applied to conventional 1-D LSMs (e.g., Sawada et al. 2015; Qin et al. 2009)
461 and lumped hydrological models (e.g., Yan and Moradkhani 2016; Vrugt et al. 2013).
462 Although particle filtering in the high dimensional system suffers from the “curse of
463 dimensionality” (e.g., Snyder et al. 2008), the applicability of particle filtering to the 3-D
464 hyperresolution land models should be assessed in the future.

465

466 Since the synthetic numerical experiment implemented in this paper assumed the extreme
467 heterogeneity of rainfall, the findings of this paper may be exaggerated. In the future work,
468 the contributions of the topography-driven surface runoff process to the data assimilation
469 of hydrological observations should be quantified in the real-world application. In
470 addition, in the virtual experiment of this paper, I neglected some of the important land
471 processes such as transpiration, canopy interception, snow, and frozen soil. Although they
472 are generally not important processes in terms of the generation of topography-driven
473 surface lateral flows, those processes should be considered in the future.

474

475

476 **6. Conclusions**

477 Lateral surface flows induced by heavy rainfalls do matter for data assimilation of soil
478 moisture observations into hyperresolution land models. Even if there is extreme
479 heterogeneity of rainfall, I can effectively propagate the information of the soil moisture
480 observations horizontally in the model space and improve the soil moisture simulation by
481 the ensemble Kalman filter. This new capability of the data assimilation with the
482 hyperresolution land models may innovate the monitor and prediction of flash floods
483 caused by local severe rainfalls. However, the non-Gaussianity of the model error induced
484 by the nonlinear dynamics of topography-driven surface flows harms the efficiency of the
485 data assimilation of soil moisture observations. When topography-driven surface slope
486 runoff exists, the efficiency of assimilating shallow soil moisture observations into the
487 hyperresolution land models depends on soil characteristics of the study area.

488

489

490 **Acknowledgement**

491 All data used in this paper are stored in the repository of Meteorological Research
492 Institute for 5 years and available upon request to Y. Sawada. The ETKF code used in this
493 study is based on the open source available at <https://github.com/takemasa-miyoshi/letkf>.
494 This study was supported by the JSPS KAKENHI grant JP17K18352.

495

496 **References**

497

498 Ait-El-Fquih, B., El Gharamti, M., & Hoteit, I. (2016). A Bayesian consistent dual
499 ensemble Kalman filter for state-parameter estimation in subsurface hydrology.
500 *Hydrology and Earth System Sciences*, 20(8), 3289–3307. [https://doi.org/10.5194/hess-](https://doi.org/10.5194/hess-20-3289-2016)
501 20-3289-2016

502

503 Amesen et al. (2013). Monitoring flood extent in the lower Amazon River floodplain
504 using ALOS/PALSAR ScanSAR images. *Remote Sensing of Environment*, 130, 51-61.
505 <https://doi.org/10.1016/j.rse.2012.10.035>

506

507 Anderson, J. L. (2007). Exploring the need for localization in ensemble data assimilation
508 using a hierarchical ensemble filter. *Physica D: Nonlinear Phenomena*, 230(1–2), 99–111.
509 <https://doi.org/10.1016/j.physd.2006.02.011>

510

511 Bandara, R., Walker, J. P., & Rüdiger, C. (2014). Towards soil property retrieval from
512 space: Proof of concept using in situ observations. *Journal of Hydrology*, 512, 27–38.
513 <https://doi.org/10.1016/j.jhydrol.2014.02.031>

514

515 Bandara, R., Walker, J. P., Rüdiger, C., & O. Merlin (2015). Towards soil property
516 retrieval from space: An application with disaggregated satellite observations. *Journal of*
517 *Hydrology*, 522, 582-593, <https://doi.org/10.1016/j.jhydrol.2015.01.018>

518

519 Beven, K. (1982), On subsurface stormflow: an analysis of response times, *Hydrological*
520 *Science Journal*, 27, 505-521, doi:10.1080/02626668209491129

521

522 Bishop, C.H., Etherton, B., J., & Majumdar, S., J., (2001). Adaptive Sampling with the
523 Ensemble Transform Kalman Filter. Part I: Theoretical Aspects. *Monthly. Weather.*

524 *Review*, **129**, 420–436, [https://doi.org/10.1175/1520-](https://doi.org/10.1175/1520-0493(2001)129<0420:ASWTET>2.0.CO;2)
525 [0493\(2001\)129<0420:ASWTET>2.0.CO;2](https://doi.org/10.1175/1520-0493(2001)129<0420:ASWTET>2.0.CO;2)

526

527 Bishop, C. H., & Hodyss, D., (2009) Ensemble covariances adaptively localized with
528 ECO-RAP. Part 1: Tests on simple error models. *Tellus*, *61A*, 84–96.

529

530 Camporese, M., Paniconi, C., Putti, M., & Salandin, P. (2009). Ensemble Kalman filter
531 data assimilation for a process-based catchment scale model of surface and subsurface
532 flow. *Water Resources Research*, *45*(10), 1–14. <https://doi.org/10.1029/2008WR007031>

533

534 Camporese, M., Paniconi, C., Putti, M., & Orlandini, S. (2010). Surface-subsurface flow
535 modeling with path-based runoff routing, boundary condition-based coupling, and
536 assimilation of multisource observation data. *Water Resources Research*, *46*(2).
537 <https://doi.org/10.1029/2008WR007536>

538

539 Crow, W. T., Van Den Berg, M. J., Huffman, G. J., & Pellarin, T. (2011). Correcting
540 rainfall using satellite-based surface soil moisture retrievals: The Soil Moisture Analysis
541 Rainfall Tool (SMART). *Water Resources Research*, *47*(8), 1–15.
542 <https://doi.org/10.1029/2011WR010576>

543

544 Fang, Y., L. R. Leung, Z. Duan, M. S. Wigmosta, R. M. Maxwell, J. Q. Chambers, & J.
545 Tomasella (2017), Influence of landscape heterogeneity on water available to tropical
546 forests in an Amazonian catchment and implications for modeling drought response, *J.*
547 *Geophys. Res. Atmos.*, *122*, doi:10.1002/2017JD027066.

548

549 Han, X., Franssen, H.-J. H., Montzka, C. & Vereecken, H. (2014). Soil moisture and soil
550 properties estimation in the Community Land Model with synthetic brightness
551 temperature observations, *Water Resources Research.*, *50*, 6081 - 6105,
552 doi:10.1002/2013WR014586.

553

554 Herrnegger, M., Nachtnebel, H. P., & Schulz, K. (2015). From runoff to rainfall : inverse
555 rainfall – runoff modelling in a high temporal resolution, 4619–4639.
556 <https://doi.org/10.5194/hess-19-4619-2015>

557

558 He, L., Hong, Y., Wu, X., Ye, N., Walker, J. P. & Chen, X. (2018). Investigation of SMAP
559 Active–Passive Downscaling Algorithms Using Combined Sentinel-1 SAR and SMAP

560 Radiometer Data. *IEEE Transactions on Geosciences and Remote Sensing*, 56, 4906-
561 4918, doi: [10.1109/TGRS.2018.2842153](https://doi.org/10.1109/TGRS.2018.2842153).

562

563 Hendricks Franssen, H. J., & Kinzelbach, W. (2008). Real-time groundwater flow
564 modeling with the Ensemble Kalman Filter: Joint estimation of states and parameters and
565 the filter inbreeding problem. *Water Resources Research*, 44(9), 1–21.
566 <https://doi.org/10.1029/2007WR006505>

567

568 Houborg, R., Rodell, M., Li, B., Reichle, R., & Zaitchik, B. F. (2012). Drought indicators
569 based on model-assimilated Gravity Recovery and Climate Experiment (GRACE)
570 terrestrial water storage observations. *Water Resources Research*, 48(7).
571 <https://doi.org/10.1029/2011WR011291>

572

573 Houtekamer, P. L., & Zhang, F. (2016). Review of the Ensemble Kalman Filter for
574 Atmospheric Data Assimilation. *Monthly Weather Review*, MWR-D-15-0440.1.
575 <https://doi.org/10.1175/MWR-D-15-0440.1>

576

577 Hunt, B. R., Kostelich, E. J., & Szunyogh, I. (2007). Efficient data assimilation for
578 spatiotemporal chaos: A local ensemble transform Kalman filter. *Physica D: Nonlinear*
579 *Phenomena*, 230(1–2), 112–126. <https://doi.org/10.1016/j.physd.2006.11.008>

580

581 Ji, P., Yuan, X., & Liang, X. Z. (2017). Do Lateral Flows Matter for the Hyperresolution
582 Land Surface Modeling? *Journal of Geophysical Research: Atmospheres*, 1–16.
583 <https://doi.org/10.1002/2017JD027366>

584

585 Keune, J., F. Gasper, K. Goergen, A. Hense, P. Shrestha, M. Sulis, & S. Kollet (2016),
586 Studying the influence of groundwater representations on land surface-atmosphere
587 feedbacks during the European heat wave in 2003, *Journal of Geophysical Research.*
588 *Atmospheres*, 121, 13,301–13,325, doi:10.1002/2016JD025426.

589

590 Kollet, S. J., & Maxwell, R. M. (2006). Integrated surface–groundwater flow modeling:
591 A free-surface overland flow boundary condition in a parallel groundwater flow model.
592 *Advances in Water Resources*, 29(7), 945–958.
593 <https://doi.org/10.1016/j.advwatres.2005.08.006>

594

595 Kumar, S. V., Reichle, R. H., Koster, R. D., Crow, W. T., & Peters-Lidard, C. D. (2009).
596 Role of Subsurface Physics in the Assimilation of Surface Soil Moisture Observations.
597 *Journal of Hydrometeorology*, 10(6), 1534–1547.
598 <https://doi.org/10.1175/2009JHM1134.1>
599

600 Kurtz, W., He, G., Kollet, S. J., Maxwell, R. M., Vereecken, H., & Franssen, H. J. H.
601 (2016). TerrSysMP-PDAF (version 1.0): A modular high-performance data assimilation
602 framework for an integrated land surface-subsurface model. *Geoscientific Model*
603 *Development*, 9(4), 1341–1360. <https://doi.org/10.5194/gmd-9-1341-2016>
604

605 Kullback, S., & Leibler, R. A. (1951). On information and sufficiency, *The Annals of*
606 *Mathematical Statistics*, 22, 79-86
607

608 Lawrence, D. M., et al. (2011). Parameterization improvements and functional and
609 structural advances in Version 4 of the Community Land Model. *Journal of Advances in*
610 *Modeling Earth Systems*, 3(3), 1–27. <https://doi.org/10.1029/2011MS000045>
611

612 Li, B., Rodell, M., Zaitchik, B. F., Reichle, R. H., Koster, R. D., & van Dam, T. M. (2012).
613 Assimilation of GRACE terrestrial water storage into a land surface model: Evaluation
614 and potential value for drought monitoring in western and central Europe. *Journal of*
615 *Hydrology*, 446–447, 103–115. <https://doi.org/10.1016/j.jhydrol.2012.04.035>
616

617 Lievens, et al. (2017). Joint Sentinel-1 and SMAP data assimilation to improve soil
618 moisture estimates. *Geophysical Research Letters*, 44(12), 6145–6153.
619 <https://doi.org/10.1002/2017GL073904>
620

621 Martens, B., Miralles, D. G., Lievens, H., Schalie, R. Van Der, & Jeu, R. A. M. De. (2017).
622 GLEAM v3 : satellite-based land evaporation and root-zone soil moisture, *Geoscientific*
623 *Model Development*, 10, 1903–1925. <https://doi.org/10.5194/gmd-10-1903-2017>
624

625 Maxwell, R. M., & N. L. Miller (2005). Development of a Coupled Land Surface and
626 Groundwater Model. *Journal of Hydrometeorology*, 6, 233-247.
627 <https://doi.org/10.1175/JHM422.1>
628

629 Maxwell, R. M., & Condon, L. E. (2016). Connections between groundwater flow and
630 transpiration partitioning. *Science*, 353, 377-380, doi: 10.1126/science.aaf7891.

631

632 Maxwell, R. M., Condon, L. E., & Kollet, S. J. (2015). A high-resolution simulation of
633 groundwater and surface water over most of the continental US with the integrated
634 hydrologic model ParFlow v3, 923–937. <https://doi.org/10.5194/gmd-8-923-2015>

635

636 Maxwell, R. M., & Kollet, S. J. (2008). Interdependence of groundwater dynamics and
637 land-energy feedbacks under climate change, *Nature Geoscience*, *1*, 665–669.
638 <https://doi.org/10.1038/ngeo315>

639

640 Maxwell, R. M., Lundquist, J. K., Mirocha, J. D., Smith, S. G., Woodward, C. S., &
641 Tompson, A. F. B. (2011). Development of a Coupled Groundwater–Atmosphere Model.
642 *Monthly Weather Review*, *139*(1), 96–116. <https://doi.org/10.1175/2010MWR3392.1>

643

644 Nerger, L., & Hiller, W., (2013). Software for ensemble-based data assimilation systems
645 – implementation strategies and scalability. *Computers & Geosciences*. *55*, 110–118.
646 <http://dx.doi.org/10.1016/j.cageo.2012.03.026>

647

648 Niu, G. Y., Paniconi, C., Troch, P. a., Scott, R. L., Durcik, M., Zeng, X., & Goodrich, D.
649 C. (2014). An integrated modelling framework of catchment-scale ecohydrological
650 processes: 1. Model description and tests over an energy-limited watershed.
651 *Ecohydrology*, *7*(2), 427–439. <https://doi.org/10.1002/eco.1362>

652

653 Pokhrel, P., & Gupta, H. V. (2010). On the use of spatial regularization strategies to
654 improve calibration of distributed watershed models. *Water Resources Research*, *46*(1),
655 1–17. <https://doi.org/10.1029/2009WR008066>

656

657 Qin, J., Liang, S., Yang, K., Kaihotsu, I., Liu, R., & Koike, T. (2009). Simultaneous
658 estimation of both soil moisture and model parameters using particle filtering method
659 through the assimilation of microwave signal. *Journal of Geophysical Research*,
660 *114*(D15), 1–13. <https://doi.org/10.1029/2008JD011358>

661

662 Rasmussen, J., Madsen, H., Jensen, K. H., & Refsgaard, J. C. (2015). Data assimilation
663 in integrated hydrological modeling using ensemble Kalman filtering: evaluating the
664 effect of ensemble size and localization on filter performance. *Hydrology and Earth
665 System Sciences*, *19*(7), 2999–3013. <https://doi.org/10.5194/hess-19-2999-2015>

666

667 Sakamoto, T., et al. (2007). Detecting temporal changes in the extent of annual flooding
668 within the Cambodia and the Vietnamese Mekong Delta from MODIS time-series
669 imagery. *Remote Sensing of Environment*, 109, 295-313.
670 <https://doi.org/10.1016/j.rse.2007.01.011>.
671

672 Sawada, Y. & Koike, T. (2014). Simultaneous estimation of both hydrological and
673 ecological parameters in an eco-hydrological model by assimilating microwave signal,
674 *Journal of Geophysical Research – Atmospheres*, 119, 8839-8857,
675 <https://doi.org/10.1002/2014JD021536>
676

677 Sawada, Y., Koike, T., & Walker, J. P. (2015). A land data assimilation system for
678 simultaneous simulation of soil moisture and vegetation dynamics, *Journal of*
679 *Geophysical Research – Atmospheres*, 120, 5910-5930,
680 <https://doi.org/10.1002/2014JD022895>
681

682 Sawada, Y., Nakaegawa, T., & Miyoshi, T. (2018) Hydrometeorology as an inversion
683 problem: Can river discharge observations improve the atmosphere by ensemble data
684 assimilation?, *Journal of Geophysical Research - Atmospheres*, 123, 848-860,
685 <https://doi.org/10.1002/2017JD027531>
686

687 Sellers, P. J., et al. (1996). A revised land surface parameterization (SiB2) for atmospheric
688 GCMs. Part I: Model formulation. *Journal of Climate*. [https://doi.org/10.1175/1520-
689 0442\(1996\)009<0676:ARLSPF>2.0.CO;2](https://doi.org/10.1175/1520-0442(1996)009<0676:ARLSPF>2.0.CO;2)
690

691 Shrestha, P., Sulis, M., Masbou, M., Kollet, S., & Simmer, C. (2014). A Scale-Consistent
692 Terrestrial Systems Modeling Platform Based on COSMO, CLM, and ParFlow. *Monthly*
693 *Weather Review*, 142(9), 3466–3483. <https://doi.org/10.1175/MWR-D-14-00029.1>
694

695 Snyder, C., Bengtsson, T., Bickel, P., & Anderson, J. (2008). Obstacles to High-
696 Dimensional Particle Filtering. *Monthly Weather Review*, 136(12), 4629–4640.
697 <https://doi.org/10.1175/2008MWR2529.1>
698

699 Tian, W., Li, X., Cheng, G. D., Wang, X. S., & Hu, B. X. (2012). Coupling a groundwater
700 model with a land surface model to improve water and energy cycle simulation.
701 *Hydrology and Earth System Sciences*, 16(12), 4707–4723. [https://doi.org/10.5194/hess-
702 16-4707-2012](https://doi.org/10.5194/hess-16-4707-2012)

703

704 Van Genuchten, M. T. (1980), A closed-form equation for predicting the hydraulic
705 conductivity of unsaturated soils, *Soil Science Society of America Journal*, 44, 892–898.

706

707 Verbeeck, H., Peylin, P., Bacour, C., Bonal, D., Steppe, K., & Ciais, P. (2011). fluxes in
708 Amazon forests: Fusion of eddy covariance data and the ORCHIDEE model. *Journal of*
709 *Geophysical Research*, 116(G2), 1–19. <https://doi.org/10.1029/2010JG001544>

710

711 Vrugt, J. A., ter Braak, C. J. F., Clark, M. P., Hyman, J. M., & Robinson, B. A. (2008).
712 Treatment of input uncertainty in hydrologic modeling: Doing hydrology backward with
713 Markov chain Monte Carlo simulation. *Water Resources Research*, 44, 1–15.
714 <https://doi.org/10.1029/2007WR006720>

715

716 Vrugt, J. A., ter Braak, C. J. F., Diks, C. G. H., & Schoups, G. (2013). Hydrologic data
717 assimilation using particle Markov chain Monte Carlo simulation: Theory, concepts and
718 applications. *Advances in Water Resources*, 51, 457–478.
719 <https://doi.org/10.1016/j.advwatres.2012.04.002>

720

721 Williams, J. L., & Maxwell, R. M. (2011). Propagating Subsurface Uncertainty to the
722 Atmosphere Using Fully Coupled Stochastic Simulations. *Journal of Hydrometeorology*,
723 12(4), 690–701. <https://doi.org/10.1175/2011JHM1363.1>

724

725 Yan, H., & Moradkhani, H. (2016). Combined assimilation of streamflow and satellite
726 soil moisture with the particle filter and geostatistical modeling. *Advances in Water*
727 *Resources*, 94, 364–378. <https://doi.org/10.1016/j.advwatres.2016.06.002>

728

729 Yang, K., Koike, T., Kaihotsu, I., & Qin, J. (2009). Validation of a Dual-Pass Microwave
730 Land Data Assimilation System for Estimating Surface Soil Moisture in Semiarid
731 Regions. *Journal of Hydrometeorology*, 10(3), 780–793.
732 <https://doi.org/10.1175/2008JHM1065.1>

733

734 Yang, K., Watanabe, T., Koike, T., Li, X., Fujii, H., Tamagawa, K., & Ishikawa, H. (2007).
735 Auto-calibration System Developed to Assimilate AMSR-E Data into a Land Surface
736 Model for Estimating Soil Moisture and the Surface Energy Budget. *Journal of the*
737 *Meteorological Society of Japan*, 85A, 229–242. <https://doi.org/10.2151/jmsj.85A.229>

738

739 Zhang, F., Snyder, C., & Sun, J. (2004). Impacts of Initial Estimate and Observation
740 Availability on Convective-Scale Data Assimilation with an Ensemble Kalman Filter.
741 *Monthly. Weather. Review.*, **132**, 1238–1253, [https://doi.org/10.1175/1520-
742 0493\(2004\)132<1238:IOIEAO>2.0.CO;2](https://doi.org/10.1175/1520-0493(2004)132<1238:IOIEAO>2.0.CO;2)

743

744 Zhang, H., Kurtz, W., Kollet, S., Vereecken, H., & Franssen, H. J. H. (2018). Comparison
745 of different assimilation methodologies of groundwater levels to improve predictions of
746 root zone soil moisture with an integrated terrestrial system model. *Advances in Water
747 Resources*, *III*(May 2017), 224–238. <https://doi.org/10.1016/j.advwatres.2017.11.003>

748

749

750

751

752

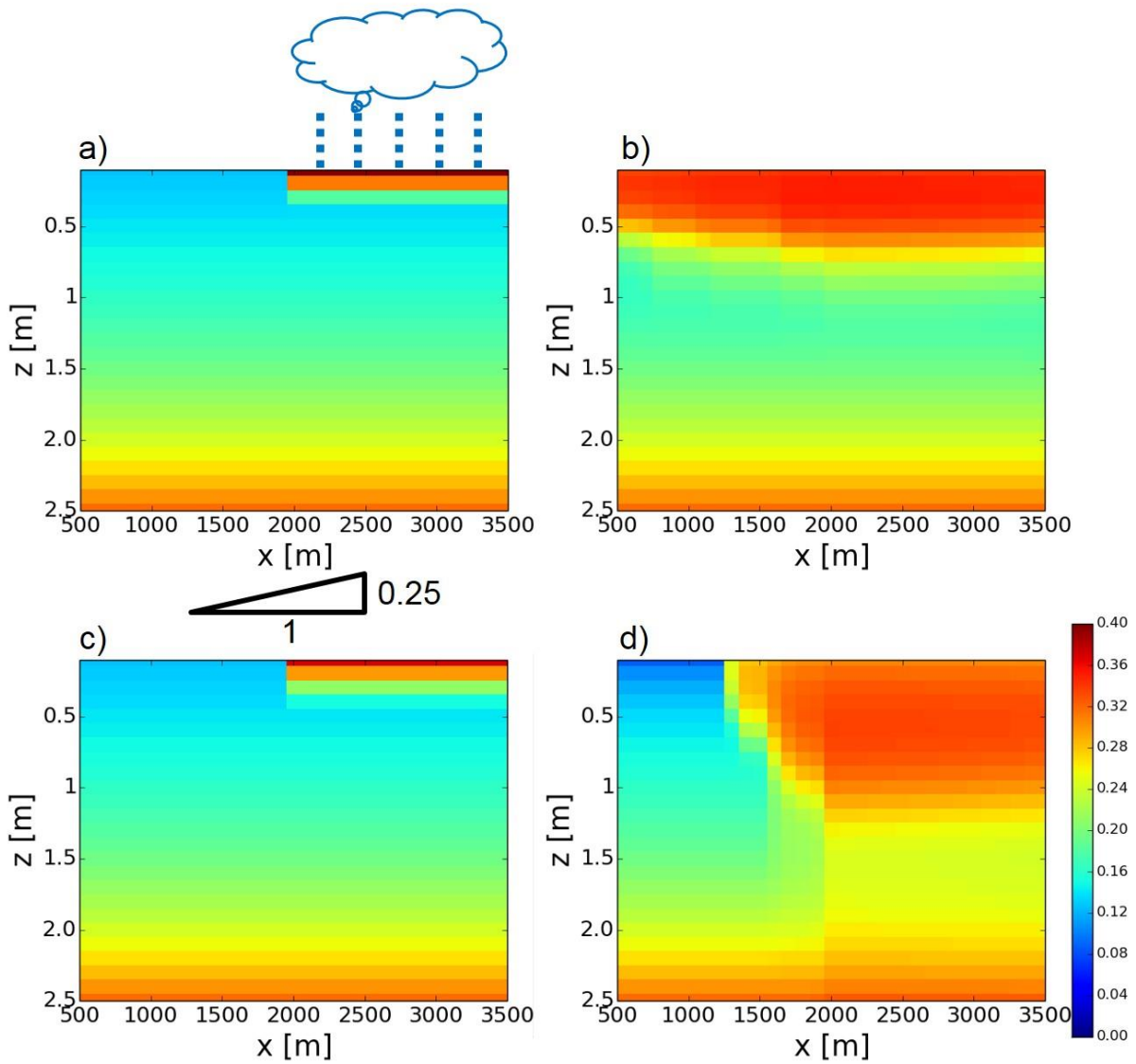
753

Table 1. Configuration of the data assimilation experiments

	hydraulic conductivity [m/h]	observation's location [m]
LOW_K-UP_O	0.005	2500
LOW_K-DOWN_O	0.005	1500
HIGH_K-UP_O	0.02	2500
HIGH_K-DOWN_O	0.02	1500

754

755



757

758

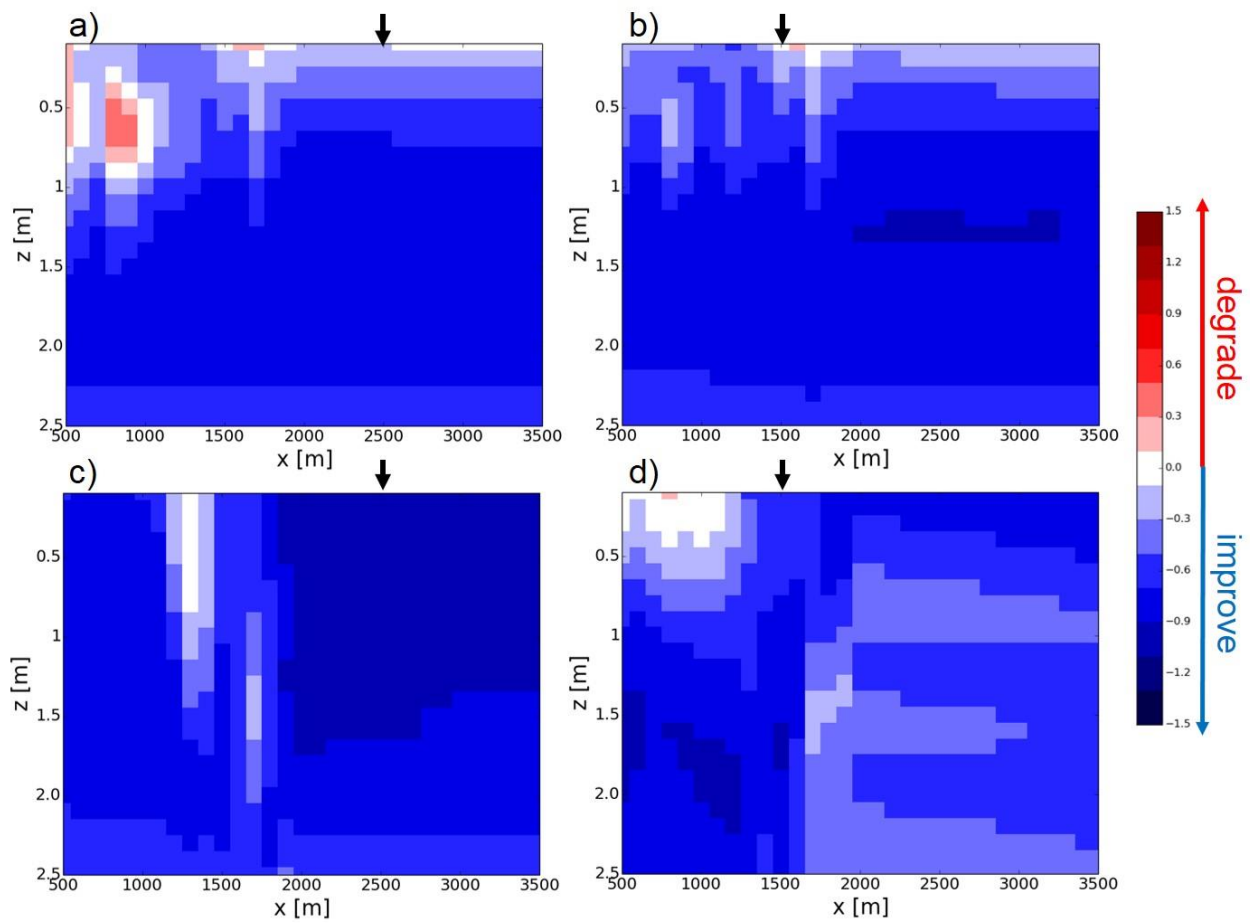
759

760

761

762

Figure 1. Distributions of volumetric soil moisture simulated by the synthetic reference runs. (a) The distribution of volumetric soil moisture [m^3/m^3] simulated by the LOW_K synthetic reference run at $t = 0\text{h}$. The schematic of the configuration of the synthetic reference runs is also shown (see also section 3). (b) same as (a) but at $t = 130\text{h}$. (c,d) same as (a,c) but for the HIGH_K synthetic reference run.



763

764

Figure 2. The improvement rates of the (a) LOW_K-UP_O, (b) LOW_K-DOWN_O, (c) HIGH_K_UP_O,

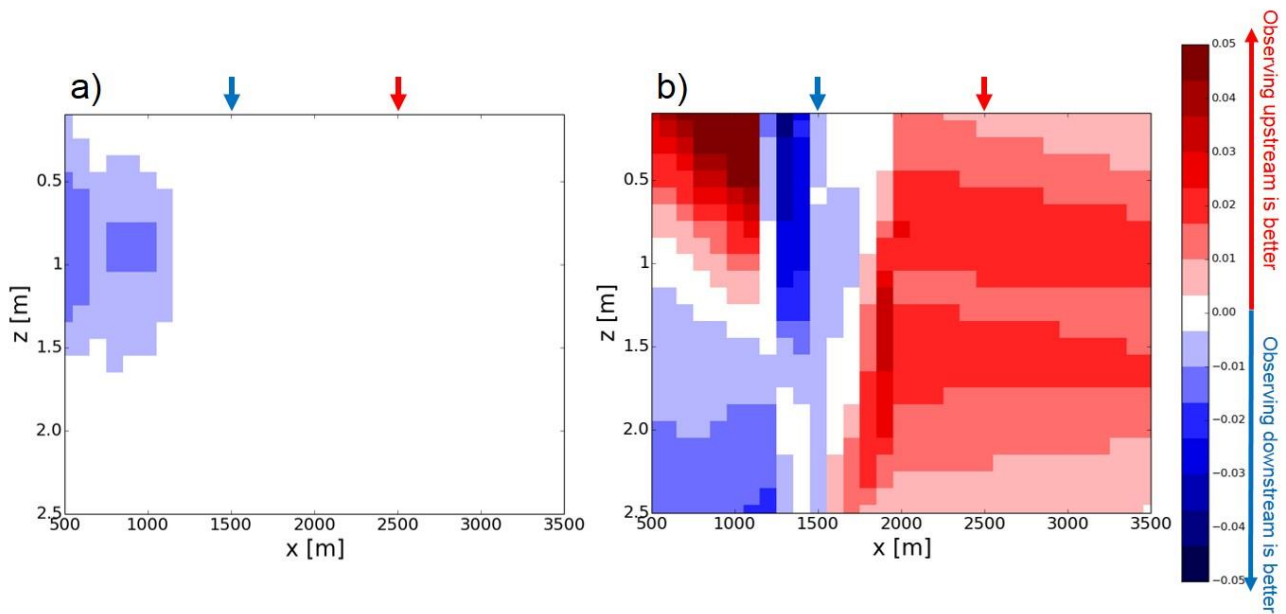
765

(d) HIGH_K-DOWN_O experiments (see Table 1 and section 3). Black arrows show the locations of the soil

766

moisture observations in each experiment.

767



768

769

770

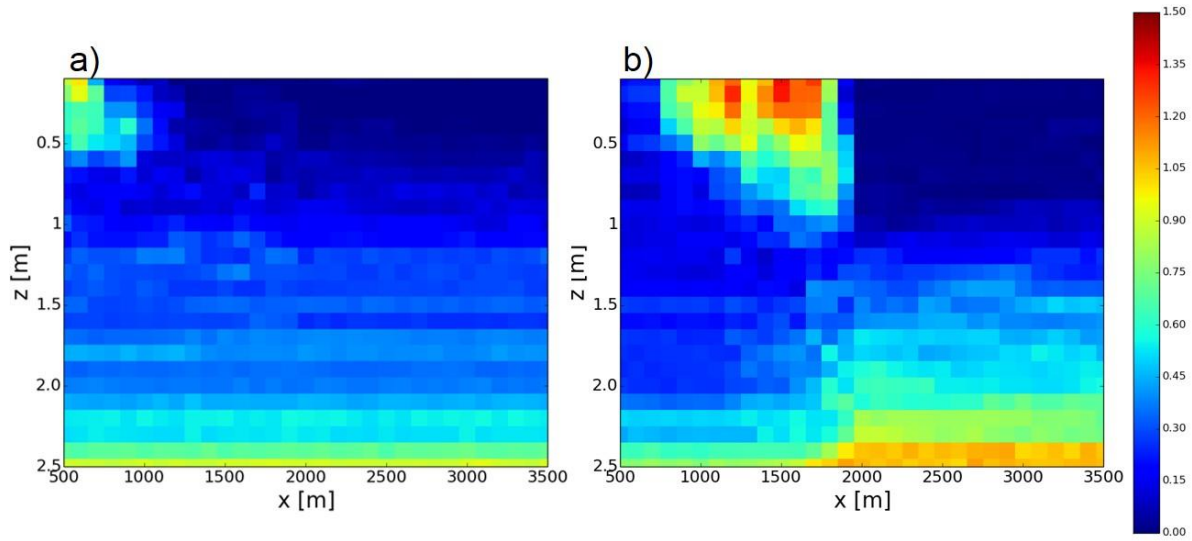
771

772

773

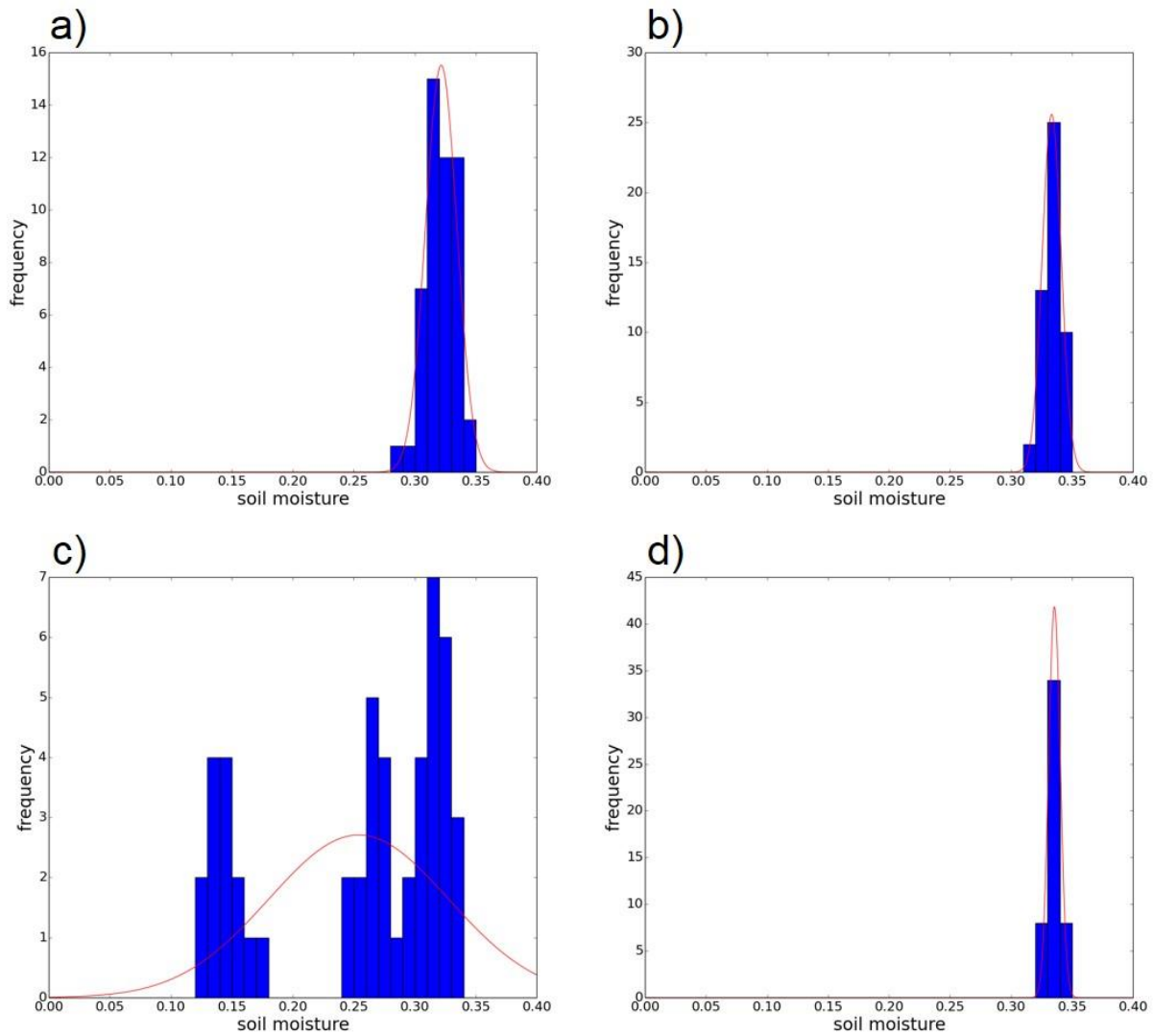
774

Figure 3. (a) The difference of time-mean RMSEs between the LOW_K-UP_O and LOW_K-DOWN_O experiments (see Table 1 and section 3). Red (blue) color indicates that the observations in the upper (lower) part of the slope reduce time-mean RMSE by data assimilation better than those in the lower (upper) part of the slope (see also arrows which are the locations of the observations). (b) same as (a) but for the difference between the HIGH_K-UP_O and HIGH_K-DOWN_O experiments.



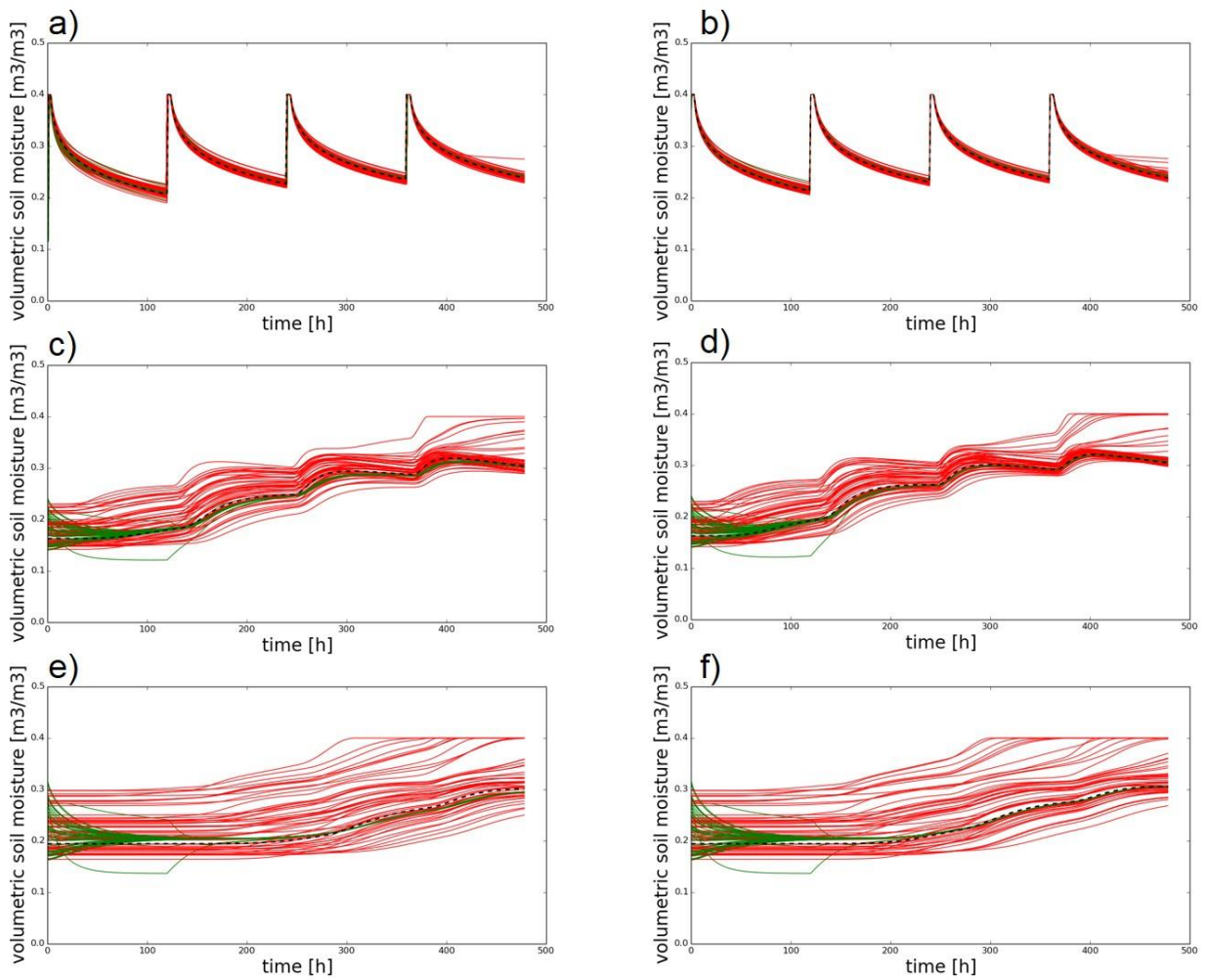
775
776
777
778

Figure 4. The Kullback-Leibler divergence of the NoDA experiment generated by (a) the LOW_K reference and (b) the HIGH_K reference at $t = 130\text{h}$ (see also Figure 1b and 1d).



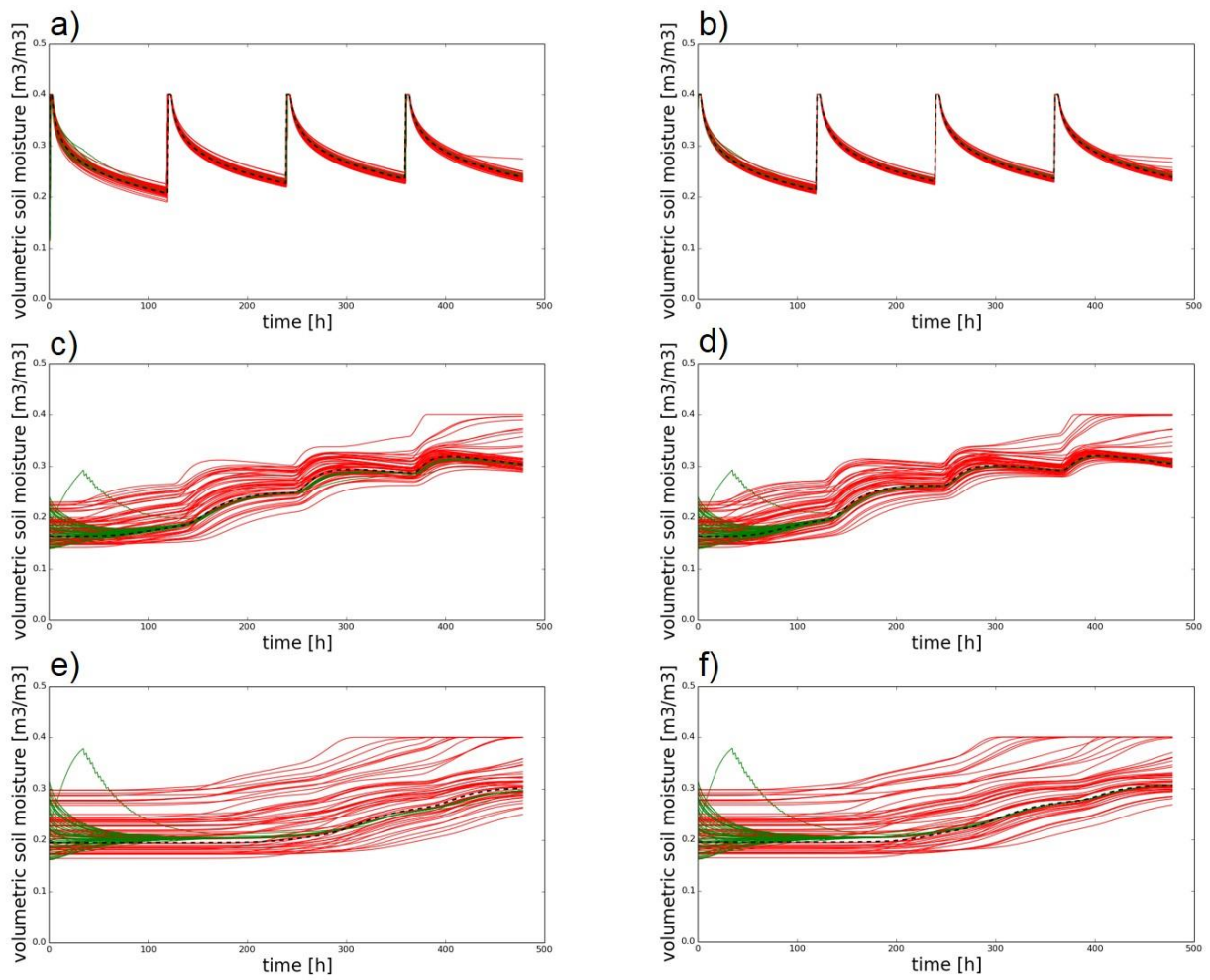
779
780
781
782
783
784
785

Figure 5. (a) The histogram (blue bars) of the volumetric soil moisture simulated by the NoDA experiment (see section 3) with the LOW_K reference at $x=1500\text{m}$, $z=0.5\text{m}$, and $t=130\text{h}$ (see also Figure 4). Red line shows the Gaussian distribution with the mean and variance sampled by the ensemble. (b) same as (a) but at $x=2500\text{m}$, $z=0.5\text{m}$, and $t=130\text{h}$. (c) same as (a) but for the HIGH_K reference. (d) same as (c) but at $x=2500\text{m}$, $z=0.5\text{m}$, and $t=130\text{h}$.



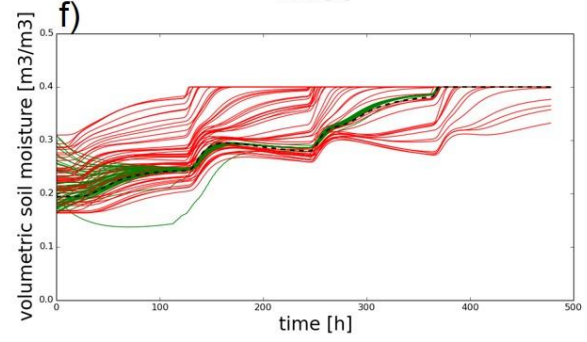
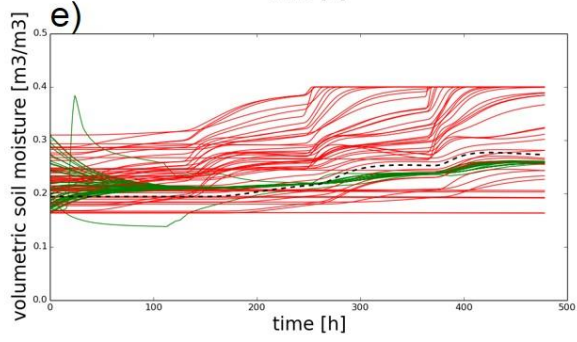
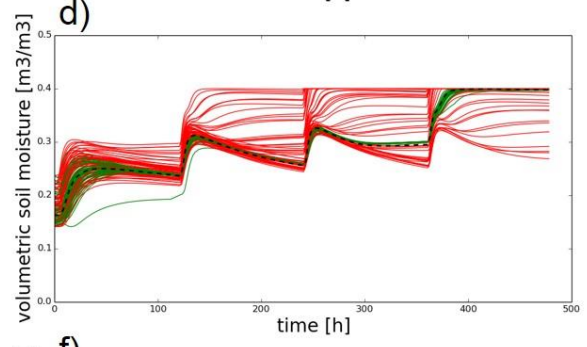
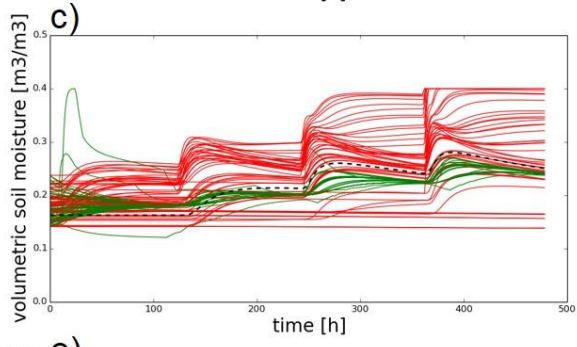
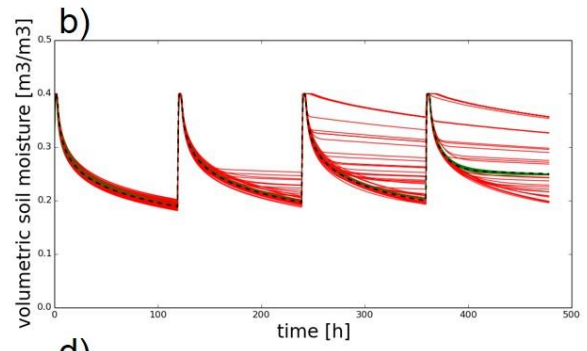
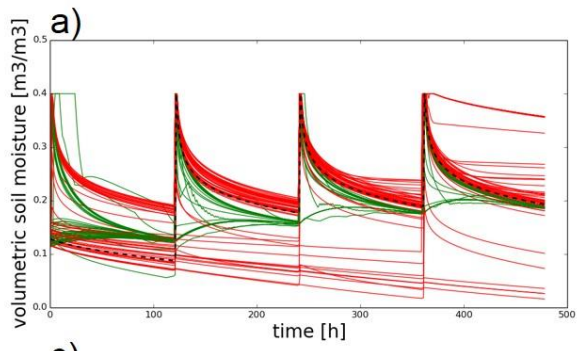
786
787
788
789
790
791

Figure S1. Time series of volumetric soil moisture simulated by the synthetic reference run (black dashed line), the NoDA experiment (red lines), and the DA experiment (green lines) in the LOW_K-UP_O experiment at a) $x=1500\text{m}, z=0.05\text{m}$; b) $x=2500\text{m}, z=0.05\text{m}$; c) $x=1500\text{m}, z=1.0\text{m}$; d) $x=2500\text{m}, z=1.0\text{m}$; e) $x=1500\text{m}, z=1.5\text{m}$; f) $x=2500\text{m}, z=1.5\text{m}$.



792
 793
 794

Figure S2. Same as Figure S1 but for the LOW_K-DOWN_O experiment.

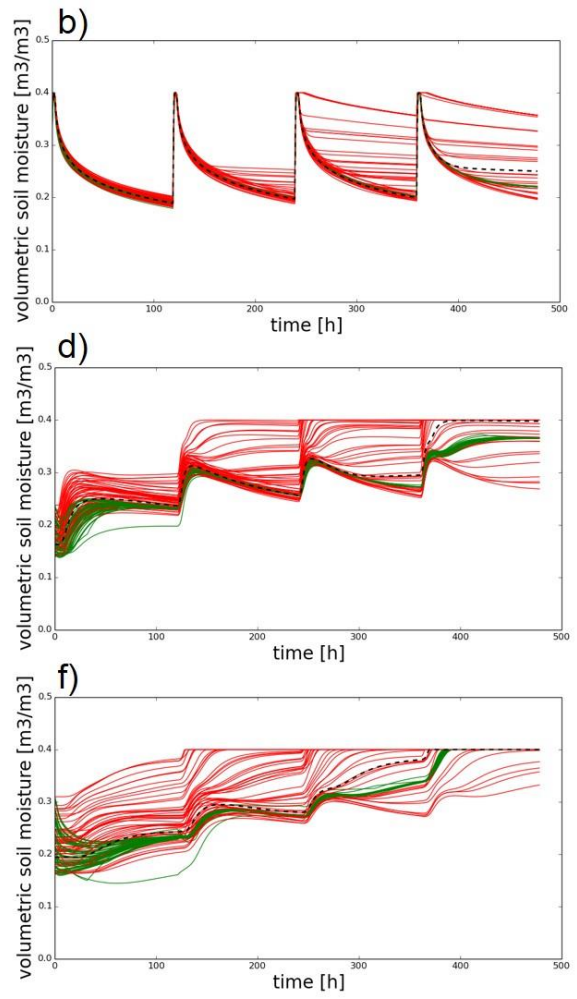
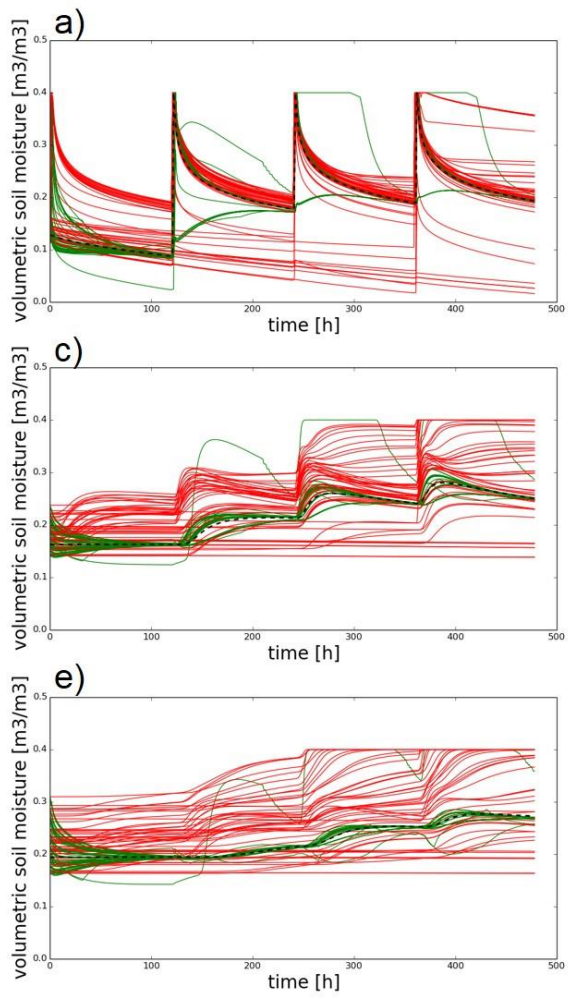


795

796

Figure S3. Same as Figure S1 but for the HIGH_K-UP_O experiment.

797



798
799
800

Figure S4. Same as Figure S1 but for the HIGH_K-DOWN_O experiment.